AGU PUBLICATIONS

JGR

Journal of Geophysical Research: Solid Earth

RESEARCH ARTICLE

10.1002/2017JB014035

Key Points:
- Postseismic deformation is recorded for 3.5 years following the 2012 M_w 7.6 Nicoya earthquake in Costa Rica
- Up to 1.7 m of afterslip is observed at the periphery of coseismic slip and near the Gulf of Nicoya
- Afterslip and aftershocks appear to be anticorrelated and potentially linked to fault properties or subducted structures

Supporting Information:
- Supporting Information S1

Correspondence to:
T. E. Hobbs,
tiegan.hobbs@gmail.com

Citation:
Hobbs, T. E., C. Kyriakopoulos, A. V. Newman, M. Protti, and D. Yao (2017), Large and primarily updip afterslip following the 2012 M_w 7.6 Nicoya, Costa Rica, earthquake, *J. Geophys. Res. Solid Earth*, *122*, 5712–5728, doi:10.1002/2017JB014035.

Received 27 JAN 2017
Accepted 27 JUN 2017
Accepted article online 29 JUN 2017
Published online 18 JUL 2017

©2017. American Geophysical Union. All Rights Reserved.

Large and primarily updip afterslip following the 2012 M_w 7.6 Nicoya, Costa Rica, earthquake

T. E. Hobbs[1], C. Kyriakopoulos[2], A. V. Newman[1], M. Protti[3], and D. Yao[1]

[1]School of Earth and Atmospheric Sciences, Georgia Institute of Technology, Atlanta, Georgia, USA, [2]Department of Earth Sciences, University of California, Riverside, California, USA, [3]Observatorio Vulcanológico y Sismológico de Costa Rica, Heredia, Costa Rica

Abstract We present detailed surface measurements of the first 3.5 years of postseismic deformation following the 5 September 2012 moment magnitude (M_w) 7.6 Nicoya, Costa Rica, earthquake. The dominant signal in the first 2.5 years is uniform horizontal trenchward motion totaling 7–26 cm across 40 stations. Trenchward velocity is strongly diminished by mid-2014 and appears by 2016 to have begun reversing. We invert the first 2.5 years to determine the corresponding afterslip on a detailed 3-D interface. Results show significant afterslip both updip and downdip of the main coseismic rupture zone, with as much as 1.7 m of offset in two patches at 15–20 km depth and immediately updip of the maximum coseismic slip. This updip slip represents an important mechanism to address unrelieved interseismic locking, although sufficient strain energy remains to generate up to a M_w 7.1 event near the coastline. The afterslip patches are anticorrelated with strongly clustered aftershocks at the same depth, which is indicative of varying frictional behavior along strike. An additional patch of slip is colocated with reoccurring slow-slip events beneath the Gulf of Nicoya. The magnitude of the observed slip, however, cannot be sufficiently explained by the known slow-slip events. Ongoing measurements will be crucial to understanding the relocking process in Nicoya.

1. Introduction

In the quest to understand the seismic cycle, much attention is paid to coseismic motions and their potential precursors. While often less destructive, postseismic processes largely control deformation in the years to decades following a large earthquake [e.g., *Khazaradze et al.*, 2002; *Hu et al.*, 2004; *Wang et al.*, 2012]. Postseismic motion results from the combined effects of: afterslip, the aseismic continuation of coseismic motion; poroelastic relaxation, short-lived deformation related to postseismic porefluid flow; viscoelastic relaxation, the long-term inelastic response of the mantle to coseismic stress; and relocking, the return to more stable interseismic accumulation of strain energy [*Wang et al.*, 2012]. Accounting for these processes is crucial to accurately estimate the accumulation of stress at later stages of the seismic cycle, that in turn improve assessments for earthquake and tsunami potential. To be reliable, postseismic deformation measurements require techniques sensitive enough to record small changes in position over years to decades that span an area of several thousand square kilometers or more. This is unavailable in the majority of subduction zones, where the seismogenic portion of the fault exists offshore and/or where funding prohibits operation of a temporally and spatially dense network.

Figure 1 highlights why the Nicoya Peninsula is particularly well situated to study a myriad of subduction zone processes. The Nicoya Peninsula sits immediately above the seismogenic zone and extends to within 60 km of the trench, allowing measurements of crustal motions to be taken from much closer to their source regions than would be possible in most other areas. As a result of this land geometry, Nicoya has been the focus of numerous geophysical investigations over the past 20 years. Previous studies have utilized seismic [e.g., *Newman et al.*, 2002; *DeShon et al.*, 2006; *Dinc et al.*, 2010] and geodetic networks [e.g., *LaFemina et al.*, 2009; *Feng et al.*, 2012; *Dixon et al.*, 2014], ocean drilling [e.g., *Vannucchi et al.*, 2001; *Davis et al.*, 2015], heat flow measurements [e.g., *Harris and Wang*, 2002; *Harris et al.*, 2010], and geomorphological observations [e.g., *Marshall and Anderson*, 1995; *Sak et al.*, 2009; *Protti et al.*, 2014] to characterize the megathrust in detail.

Convergence of the Cocos and Caribbean plates is sufficiently rapid to generate $M \geq 7$ earthquakes beneath the peninsula roughly every 50 years since 1853 [*Protti et al.*, 1995; *Feng et al.*, 2012]. In addition to these larger earthquakes, the Nicoya megathrust exhibits persistent tremor activity and very low frequency microseismicity updip and downdip of the seismogenic zone [*Walter et al.*, 2011, 2013]. The low-frequency

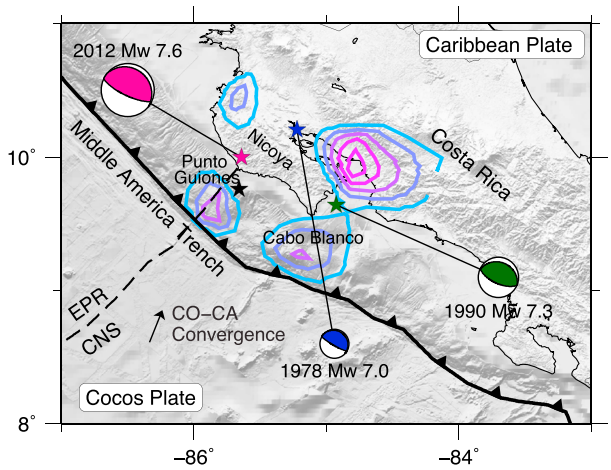

Figure 1. Tectonic configuration of Nicoya study area, with Cocos Plate subducting beneath Caribbean Plate along the Middle America Trench in azimuth shown at a rate of 7.7 cm/yr [*DeMets et al.*, 2010]. Transition is shown from oceanic crust sourced at the East Pacific Rise (EPR) and Cocos-Nazca Spreading Center (CNS) [*Barckhausen et al.*, 2001]. At this location there is a transition from steep subduction of relatively cold EPR crust to the more shallowly downgoing and warmer CNS crust. Slow-slip contours of *Dixon et al.* [2014] shown from blue to pink in 100 cm intervals. Centroid [*Ekström et al.*, 2012] and relocated hypocenter [*Yue et al.*, 2013] for 2012 M_w 7.6 Nicoya earthquake shown by pink and black stars, respectively. The 1990 M_w 7.0 Gulf of Nicoya earthquake [*Protti et al.*, 1995] shown in green, and 1978 M_w 7.0 Samara earthquake [*International Seismological Centre*, 2014] shown in blue. Global centroid-moment tensor solutions [*Ekström et al.*, 2012] shown by beachballs, scaled by magnitude. Fisher Seamount Chain can be seen from bathymetry beneath the word "convergence," heading toward the southern tip of the Nicoya peninsula.

earthquakes and tremor are sometimes coincident with slow-slip events (SSEs) occurring about once a year between 2007 and 2012 [*Outerbridge et al.*, 2010; *Jiang et al.*, 2012; *Dixon et al.*, 2014]. This measurable complexity of fault behavior has established Nicoya as a rich natural laboratory for subduction zone studies (see http://nicoya.eas.gatech.edu for more information).

The most recent large earthquake was the 5 September 2012 moment magnitude (M_w) 7.6 Nicoya earthquake (Figure 1), which was preceded by a 9 day foreshock sequence [*Walter et al.*, 2015]. This event nucleated 10 km offshore at 13 km depth along the interface [*Yue et al.*, 2013], with rupture concentrating downdip and beneath the peninsula [*Yue et al.*, 2013; *Protti et al.*, 2014; *Liu et al.*, 2015; *Kyriakopoulos and Newman*, 2016]. The approximately 110 by 50 km coseismic rupture area [*Liu et al.*, 2015] is shown by *Protti et al.* [2014] to roughly align with the region of significant (≥50%) previous interseismic locking [*Feng et al.*, 2012]. A potential zone of unreleased slip in the *Protti et al.* [2014] model, located immediately offshore and north west of the hypocenter [*Protti et al.*, 2014, Figure 4b], was shown by *Kyriakopoulos and Newman* [2016] to be partially diminished in amplitude and spatial extent when a fully 3-D slab geometry is implemented. It is expected that postseismic slip will release much of this remaining strain energy, effectively balancing the slip budget before Nicoya enters a new seismic cycle.

Here we use a novel data set of campaign and continuous land-based Global Positioning System (GPS) observations on and near the Nicoya Peninsula to measure ongoing postseismic deformation from 2012 to 2016. These data directly record the timing and spatial extent of surface deformation from the combined postseismic processes. Geodetic inversions are carried out and compared spatially against interseismic and coseismic fault slip, aftershocks, and cumulative slow slip to establish the contribution of postseismic phenomena to the seismic cycle budget. Insights from well-instrumented locations like Nicoya are critical to understanding seismic cycle behavior in subduction zones like Cascadia [*Wang and Tréhu*, 2016], which have relatively sparse near-trench coverage. In coming years, we expect to record accelerating landward motion as the subduction zone reenters an interseismic state.

2. Methods

2.1. Data Collection

Following a postearthquake deployment in 2012, field work was again completed in March 2015 and 2016 on the Nicoya Peninsula to obtain new campaign GPS data. By returning to these sites at the same time each year we minimize most seasonal variations that could otherwise affect GPS calculations. In the field campaign from 6 to 19 March 2015, GPS data were collected at 31 stations on and around the Nicoya Peninsula and Arenal volcano, with instruments recording continuously for 2–3 days at a 30 s sampling interval. Of interest to this study is the subset of 22 stations for which there are previous campaign data taken in 2012 right after the earthquake (Figure 2a, details provided in Tables 1 and 2). Postprocessing of the raw data is completed

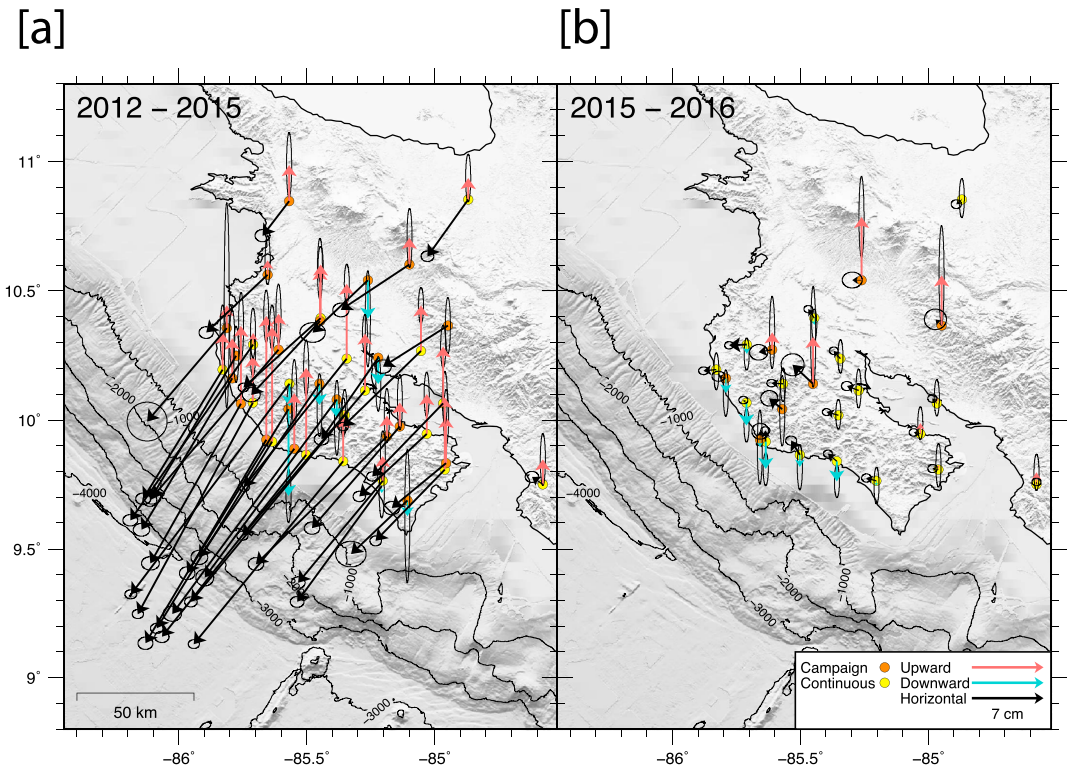

Figure 2. Displacement, relative to Caribbean plate, at campaign (orange) and continuous (yellow) GPS sites for (a) 2012–2015 and (b) 2015–2016. Horizontal displacements in black, upward in red, and downward in blue. Shown are the 22 available campaign measurements from 2012–2015, compared to only seven campaign sites successfully occupied in 2016.

using the precise point positioning software "GIPSY-OASIS," made available by the Jet Propulsion Laboratory (JPL). Final fiducial-free daily solutions are determined using precise satellite orbits provided by JPL and ocean loading coefficients from the FES2004 hydrodynamic model [*Letellier*, 2005], with ambiguity resolution handled by AMBIZAP [*Blewitt*, 2008]. March 2016 measurements followed the same procedure for a subset of seven campaign sites in the central peninsula, focusing on stations with poorer coverage during the 2015 campaign (Figure 2b).

These data follow the most recent prior campaign conducted in 2012, in rapid response to the 5 September 2012 Nicoya earthquake [*Protti et al.*, 2014]. Instruments were deployed between 8 and 22 September 2012, with all units recording a minimum of three complete coordinated universal time days. Several stations (COBA, DIRI, GUIO, MATA, and MIRM) were left in continuous mode to measure several consecutive months of postseismic deformation.

In addition to campaign measurements, data were also collected from a network of 18 continuously recording GPS stations on and near the Nicoya Peninsula. This network is operated by the University of South Florida and the Observatorio Vulcanológico y Sismológico de Costa Rica, with technical support from University NAVSTAR Consortium (UNAVCO) (http://www.unavco.org) (Tables 1 and 2). Shown in Figure 3, time series of daily position solutions are created for a subset of continuous GPS station daily solutions for which there was good temporal coverage. It is immediately evident that there is a strongly nonlinear displacement in the first several months, which flattens out at most stations by approximately 2014. By the start of 2015 most stations appear to show a gentle reversal in direction of their initial postseismic motion, continuing until at least the end of the time series (31 May 2016).

Due to the sparsity of the data points for campaign measurements, nonlinear postseismic velocities cannot be well constrained at each site. Instead, cumulative offsets are computed at all 40 stations by differencing start and end positions for the time periods: 2.5 years from immediately following the earthquake to March 2015, and 1 year from March 2015 to March 2016 (to match timing of campaign measurements). Only daily positions with formal horizontal error of less than 1 cm are used in calculating displacement.

Table 1. Displacements and Errors From 2012 to 2015 at Campaign and Continuous GPS Stations Used in This Study[a]

Station	Longitude	Latitude	Elev. (m)	Start	End	E (mm)	eE (mm)	N (mm)	eN (mm)	U (mm)	eU (mm)
Campaign											
BAGA	−85.261	10.5414	123.49	2012.7022	2015.1945	−53.87	5.06	−51.08	3.91	−37.67	19.07
BALL	−85.448	10.3834	118.03	2012.7077	2015.1836	−67.01	3.54	−71.98	2.85	50.80	12.19
BONG	−85.207	9.7438	21.54	2012.6940	2015.1945	−82.47	2.75	−112.97	2.18	−7.01	9.79
CEBA	−85.776	10.2491	90.43	2012.6967	2015.1863	−84.13	2.78	−140.81	2.54	1.28	11.16
COBA	−85.107	9.6881	172.44	2012.7240	2015.1890	−55.06	6.08	−52.37	5.08	−15.35	26.49
DIRI	−85.611	10.2718	82.04	2012.6940	2015.1781	−123.10	3.47	−143.86	2.72	35.10	11.81
GRAN	−85.653	10.5622	122.24	2012.7022	2015.1890	−59.94	2.84	−56.37	2.34	14.25	9.72
GUA2	−85.450	10.1401	136.32	2012.6913	2015.1781	−117.24	3.34	−169.28	2.81	−20.76	12.53
GUIO	−85.659	9.9231	31.42	2012.6913	2015.1808	−117.78	2.97	−198.44	2.47	120.61	10.35
HOJA	−85.382	10.0795	240.97	2012.6858	2015.1808	−128.77	3.57	−173.65	3.36	−17.86	14.84
JICA	−85.136	9.9751	61.40	2012.6995	2015.1863	−85.65	3.11	−99.23	2.44	23.58	10.97
LEON	−85.187	9.9365	276.91	2012.6885	2015.1836	−127.69	3.09	−124.48	2.55	20.31	10.78
MATA	−85.813	10.3553	77.82	2012.6967	2015.2000	−77.63	7.96	−91.02	7.73	22.22	40.87
MIRM	−85.571	10.0421	433.75	2012.7158	2015.1890	−98.85	3.10	−160.09	2.55	−84.69	10.54
PALO	−85.220	10.2415	40.05	2012.7022	2015.1836	−55.40	2.92	−79.54	2.33	−25.66	10.77
PAQU	−84.955	9.8322	80.26	2012.7049	2015.1918	−53.02	3.21	−43.76	2.63	45.06	11.02
POTR	−85.569	10.8474	155.76	2012.7131	2015.1945	−25.89	2.98	−33.78	2.43	35.07	12.96
SAMA	−85.549	9.8892	45.91	2012.6913	2015.1781	−118.93	3.66	−161.10	3.00	54.37	13.21
SJOS	−84.948	10.3656	1062.14	2012.6995	2015.2000	−63.25	3.28	−39.97	2.68	−0.01	11.14
SJUA	−85.757	10.0632	44.58	2012.7104	2015.1863	−88.38	3.55	−155.78	2.66	76.04	13.12
TENO	−85.098	10.6018	373.35	2012.7131	2015.2055	−66.88	3.24	−44.32	2.73	25.94	11.75
VENA	−85.792	10.1611	24.98	2012.6940	2015.1863	−88.42	3.28	−147.66	2.55	38.94	11.36
Continuous											
BIJA	−84.577	9.7500	555.54	2012.7240	2015.1945	−10.67	2.68	7.40	2.19	24.37	10.27
BON2	−85.203	9.7645	28.33	2012.7049	2015.1945	−82.46	2.71	−99.36	2.31	24.24	9.95
CABA	−85.344	10.2379	26.78	2012.6803	2015.1945	−100.13	2.21	−125.06	1.81	73.06	7.72
ELVI	−85.446	10.3947	81.76	2012.7131	2015.1945	−75.29	2.09	−67.71	1.73	52.46	7.13
EPZA	−85.568	10.1409	668.60	2012.6803	2015.5671	−154.62	2.37	−205.49	1.79	−22.13	7.90
GRZA	−85.636	9.9155	39.69	2012.6967	2015.1945	−112.42	2.53	−181.98	2.00	111.81	8.79
HATI	−85.710	10.2922	58.69	2012.6803	2015.1945	−119.69	2.95	−171.40	2.27	11.24	9.91
HUA2	−85.352	10.0177	594.20	2012.6831	2015.1945	−150.02	2.53	−181.89	1.99	3.94	8.64
IND1	−85.502	9.8646	75.44	2012.6858	2015.1945	−140.75	2.86	−177.53	2.23	84.93	11.09
LAFE	−84.960	9.8071	65.17	2012.6803	2015.1945	−67.42	2.29	−69.41	1.97	70.43	10.32
LEPA	−85.031	9.9454	20.97	2012.7077	2015.1945	−65.70	2.47	−60.85	2.07	38.80	8.74
LMNL	−85.053	10.2675	102.85	2012.6803	2015.1945	−76.01	2.09	−73.74	1.69	44.52	7.07
PNE2	−85.829	10.1952	19.66	2012.7049	2015.1945	−77.53	3.01	−126.03	2.28	36.17	11.01
PUJE	−85.273	10.1140	29.10	2012.6803	2015.6411	−119.52	2.23	−141.66	1.79	55.46	7.54
PUMO	−84.967	10.0645	17.90	2012.6803	2015.1945	−69.20	2.23	−71.35	1.82	55.56	8.45
QSEC	−85.357	9.8404	17.74	2012.6803	2015.1945	−145.74	2.22	−178.47	1.75	42.87	7.70
SAJU	−85.711	10.0671	73.82	2012.6803	2015.1945	−112.18	2.23	−206.19	1.81	45.58	7.91
VERA	−84.869	10.8536	64.30	2012.6803	2015.1945	−39.70	2.53	−55.49	2.10	20.99	9.49

[a]Dates in decimal years, displacements relative to stable Caribbean plate.

Earliest postseismic positions are taken as the average position over the first 2 days of available postseismic recordings, corresponding to the date used in *Protti et al.* [2014] to define the end of coseismic displacement. For the 2015 and 2016 campaigns we average over all available days, up to four. Continuous data sets are sampled using a 4 day window corresponding to the average timing of the campaign measurements. The start period of 2 days was chosen to retain as much of the early postseismic signal as possible. Displacements at each station were converted from ITRF2008 reference frame [*Altamimi et al.*, 2011], to a stable Caribbean plate using *DeMets et al.* [2010]. Beginning and end times, as well as displacements for each station, are given in Table 1 for 2012–2015 and Table 2 for 2015–2016.

As we do not capture the first hours to days of afterslip, measurements herein are a lower bound on total afterslip, emphasizing the spatial distribution of slip over the course of several years. However, our 2012 "start" date reflects the "end" date of previous coseismic geodetic studies [*Protti et al.*, 2014; *Kyriakopoulos and Newman*, 2016], allowing for direct comparison between those results and our observed postseismic deformation. For a discussion of earliest afterslip from high-rate GPS please see *Malservisi et al.* [2015]. While we do not account for aftershocks independently, their contribution to total slip is included in and discussed in our results.

Table 2. Displacements and Errors From 2015 to 2016 at Campaign and Continuous GPS Stations Used in This Study[a]

Station	Longitude	Latitude	Elevation (m)	Start	End	E (mm)	eE (mm)	N (mm)	eN (mm)	U (mm)	eU (mm)
Campaign											
BAGA	−85.261	10.541	123.49	2015.186	2016.180	−9.02	3.97	0.12	3.16	61.84	16.12
DIRI	−85.611	10.272	82.04	2015.175	2016.175	−13.13	3.61	−2.45	3.09	16.96	14.36
GUA2	−85.450	10.140	136.32	2015.175	2016.169	−20.03	4.58	18.59	4.38	45.92	20.08
GUIO	−85.659	9.923	31.42	2015.178	2016.169	0.35	3.35	8.36	3.16	−7.11	14.72
MIRM	−85.571	10.042	433.75	2015.175	2016.169	−12.63	3.40	10.56	3.06	−1.66	14.01
SJOS	−84.948	10.366	1062.14	2015.197	2016.178	−5.97	4.40	6.10	4.10	48.91	19.89
VENA	−85.792	10.161	24.98	2015.184	2016.175	−7.12	2.60	2.04	1.99	−14.32	9.20
Continuous											
BIJA	−84.577	9.750	555.54	2015.175	2016.178	−0.08	1.81	2.42	1.51	11.76	7.21
BON2	−85.203	9.765	28.33	2015.175	2016.178	−9.85	1.90	2.63	1.65	−4.71	7.29
CABA	−85.344	10.238	26.78	2015.175	2016.178	−6.46	1.76	7.57	1.51	2.09	6.64
ELVI	−85.446	10.395	81.77	2015.175	2016.178	−5.83	1.74	8.75	1.44	−6.44	6.21
EPZA	−85.568	10.141	668.59	2015.559	2016.178	−11.16	1.88	0.44	1.47	−1.22	6.66
GRZA	−85.636	9.916	39.69	2015.175	2016.178	−0.40	1.81	11.06	1.44	−26.81	6.49
HATI	−85.710	10.292	58.68	2015.175	2016.178	−17.17	1.76	−0.74	1.46	−9.20	6.38
HUA2	−85.352	10.018	594.20	2015.175	2016.178	−11.47	1.69	3.25	1.39	1.07	5.92
IND1	−85.502	9.865	75.14	2015.175	2016.178	−8.45	2.22	13.93	1.79	−12.04	8.97
LAFE	−84.960	9.807	65.18	2015.175	2016.178	−5.74	1.86	1.18	1.64	4.30	8.68
LEPA	−85.031	9.945	20.97	2015.175	2016.178	−6.54	1.77	1.59	1.51	10.57	6.51
PNE2	−85.829	10.195	19.66	2015.175	2016.178	−12.39	2.00	−1.17	1.52	−1.73	7.34
PUJE	−85.273	10.114	29.09	2015.175	2016.178	−11.38	2.18	4.41	1.81	2.01	7.75
PUMO	−84.967	10.065	17.91	2015.175	2016.178	−4.40	1.81	4.70	1.51	5.43	7.20
QSEC	−85.357	9.840	17.73	2015.175	2016.178	−8.73	1.77	7.35	1.42	−19.89	6.38
SAJU	−85.711	10.067	73.81	2015.175	2016.178	−3.09	1.80	2.48	1.49	−22.21	6.64
VERA	−84.869	10.854	64.31	2015.175	2016.178	−5.35	2.04	−4.64	1.75	1.29	7.78

[a]Dates in decimal years, displacements relative to stable Caribbean plate.

2.2. Afterslip Inversion

To quantify the subsurface processes responsible for postseismic displacements, we initially assume that all postseismic deformation is the result of elastic deformation of the crust caused by slip occurring exclusively on the subduction interface. Cumulative displacements over the 2015–2016 period are not considered for inversion, as the magnitude of deformation is small and the data are limited (Figure 2b). *GTdef* [*Chen et al.*, 2009] is used to perform an inversion of the 2012–2015 surface displacement vectors.

We perform a bounded, weighted linear least squares inversion, similar to previous Nicoya deformation studies [*Feng et al.*, 2012; *Protti et al.*, 2014; *Kyriakopoulos and Newman*, 2016]. For a subduction interface defined by coincident pair nodes, Green's functions are obtained for each node-station pair assuming unit slip on each patch. For surface displacement observations ($\boldsymbol{d}$) weighted ($\boldsymbol{W}$) by their errors ($\boldsymbol{d}' = \boldsymbol{Wd}$), the weighted Green's functions ($\boldsymbol{G}' = \boldsymbol{WG}$) are used to solve the linear system $\boldsymbol{d}' = \boldsymbol{G}'\boldsymbol{m}$ for slip on the interface ($\boldsymbol{m}$) [*Jónsson et al.*, 2002; *Feng et al.*, 2012; *Kyriakopoulos and Newman*, 2016].

Allowing hundreds of fault solutions with independent slips results in an underdetermined problem for the 120 observations available (40 stations, each with three components). To allay this and avoid unrealistic variations in slip over small distances on the fault, the full inversion also applies smoothing conditions along strike and dip:

$$\begin{bmatrix} \boldsymbol{d}' \\ 0 \end{bmatrix} = \begin{bmatrix} \boldsymbol{G}' \\ \kappa^2 \boldsymbol{D} \end{bmatrix} \boldsymbol{m}$$

which includes a Lagrangian smoothness weighting multiplier (κ) and the second-order Laplacian smoothing operator ($\boldsymbol{D}$) [see *Jónsson et al.*, 2002 for details]. In all cases, a Poisson's ratio of 0.25 is assumed over a range of κ values.

Generally, model misfit increases with smoothing, resulting in a trade-off between smoothness of the fault solution and residual error. This leads to a nonunique suite of results, dependent on κ, from which the preferred solution must be selected [e.g., *Gubbins*, 2004]. Most commonly, the inflection point in a curve of

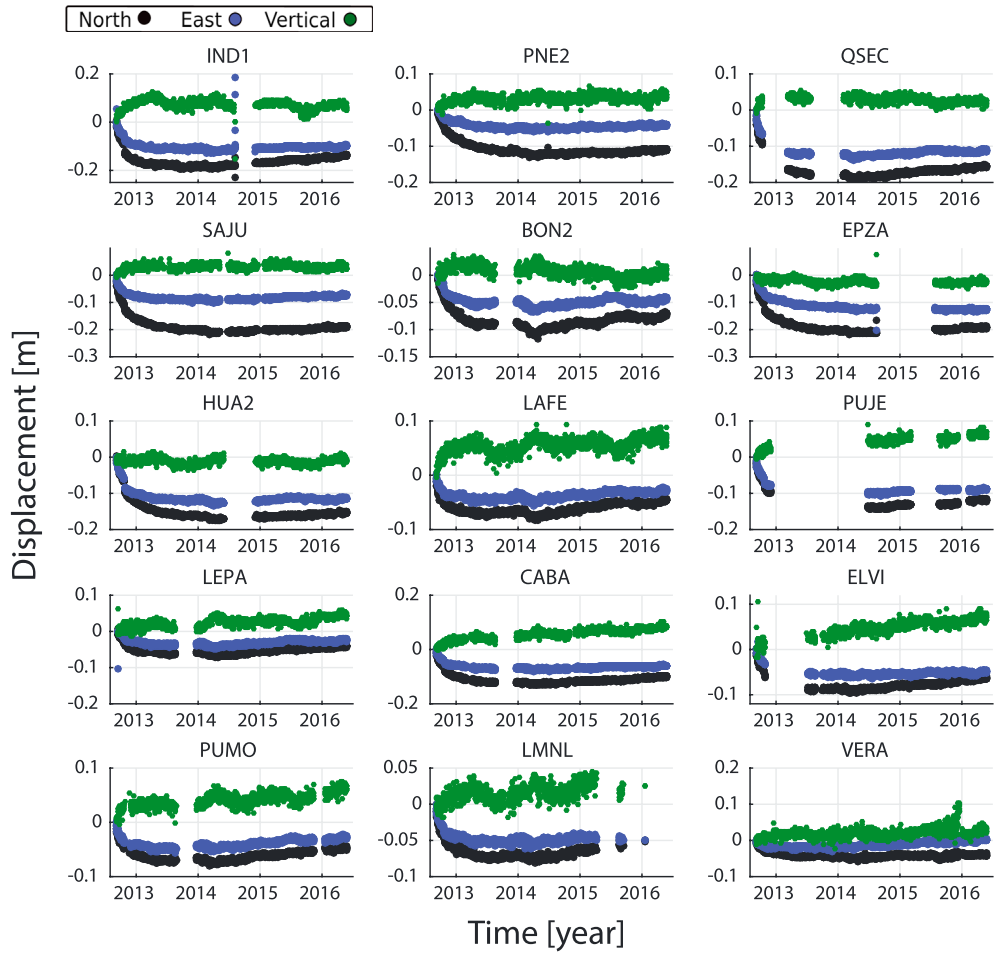

Figure 3. Displacement (meters) relative to the first day after the 2012 earthquake for a subset of continuous GPS stations having good temporal coverage. All offsets are given for a fixed Caribbean reference frame. Stations are arranged (left to right, starting from top row and working down) by distance from the trench. North, east, and vertical components are displayed in black, blue, and green, respectively. Postseismic daily displacements are large at first, diminishing with time, and ultimately reversing by approximately the start of 2015. Potential SSEs are visible as short-term reversals in direction of motion.

roughness (ρ) versus root-mean-square (RMS) misfit is subjectively chosen for a preferred solution, such that additional smoothing produces an unacceptably large increase in misfit [e.g., *Jónsson et al.*, 2002; *Chen et al.*, 2009]. Here

$$\rho = \frac{\Sigma_i |\boldsymbol{p}_i|}{2N}$$

for $\boldsymbol{p} = \boldsymbol{Dm}$ for each patch, i, for a total of N fault patches, and normally described in cm/km^2.

The inversion is performed first with a simplified, 2-D curviplanar geometry consistent with *Feng et al.* [2012], and then with a detailed fully 3-D model consistent with *Kyriakopoulos and Newman* [2016]. We implement high-resolution 3-D fault geometry to better represent subduction heterogeneities like the East Pacific Rise-Cocos Nazca Spreading Center (EPR-CNS) transition (Figure 1) or potential subducted seamounts [e.g., *Protti et al.*, 1995; *Husen et al.*, 2002; *Wang and Bilek*, 2011]. Specifically, we use the slab surface of *Kyriakopoulos et al.* [2015], determined using the maximum seismicity method described therein. This model, which represents the most recent, detailed characterization of the interface, is superior in Nicoya where the main coseismic rupture area straddles crustal material of heterogeneous providence [*Barckhausen et al.*, 2001]. Due to the higher resolution of the 3-D model, we leave details

of the model based on the 2-D geometry for the supporting information and Figure S1. We present the 2-D geometry to highlight that slip details are largely similar between geometries and are not substantially affected by complexity in the topographically diverse 3-D interface of *Kyriakopoulos et al.* [2015]. Subsequent discussion will correspond to the 3-D model and results.

As detailed in *Kyriakopoulos and Newman* [2016], the subduction surface is discretized into a finite element model (FEM) with 43 along-strike by 21 along-dip coincident pair nodes, each patch having an area of approximately 5 × 5 km. Maximum depth varies between 36 km in the south and 67 km at the northern edge, resulting from an angle of subduction which is dramatically steeper in the northern EPR crust [*Kyriakopoulos et al.*, 2015, Figure 6a]. Green's functions are subsequently calculated within FEM software, ABAQUS (http://www.simulia.com/). For the bounded least squares inversion, we allow up to 10 m of slip as positive thrust or as strike-slip motion in either direction. These slip limits are several times larger than expected (and ultimately modeled) postseismic slip, and more than a factor of 2 greater than the maximum coseismic slip determined to be about 4.4 m [*Protti et al.*, 2014; *Kyriakopoulos and Newman*, 2016]. The edges of the model are permitted to slip freely, except in "Fixed Surface" inversions where slip is forced to be zero at the trench. We view these two boundary conditions as end-member models, while noting that this model and network geometry are unable to resolve between the two.

Spatial recoverability is limited by the distribution of GPS stations on the Nicoya Peninsula. The spatial recoverability is evaluated by performing a checkerboard test using an input grid with a cell size of 20 × 40 km, comparable to the size of features observed. Starting with an initial model with alternating unit slip patches (1 m), split equally between strike and dip slip components, we add white Gaussian noise corresponding to the calculated GPS errors to the forward model prediction at each site. The resultant displacements, plus error, are used as input for inversions that would ideally recover the initial input checkerboard.

We also consider the model resolution matrix, used to quantify the area over which individual model parameters affect one another [e.g., *Gubbins*, 2004]. The resolution matrix, $\mathbf{R} = \mathbf{G}^{-g}\mathbf{G}$ [*Menke*, 1989], is evaluated with the generalized inverse of the weighted, damped least squares problem: $\mathbf{G}^{-g} = (\mathbf{G}^{\mathbf{T}}\mathbf{W}\mathbf{G} + \kappa\mathbf{D}^{\mathbf{T}}\mathbf{D})^{-1}\mathbf{G}^{\mathbf{T}}\mathbf{W}$ [*Jónsson et al.*, 2002; *Kyriakopoulos and Newman*, 2016]. If the inversion reproduced the true model then $\mathbf{R}$ would equal the identity matrix, but in practice the diagonals are somewhat less than 1 with nonzero off-diagonal elements representing dependence between model parameters [*Gubbins*, 2004]. The ith row of the resulting resolution matrix provides a measure of the trade-off between that parameter and all other j parameters ($j \neq i$), for a specified smoothness weighting. A useful characterization of the resolution matrix is a scalar field of the resolution spread parameter, r, described as

$$r_i = \frac{L_i}{\sqrt{R_i}}$$

for patch length L_i and diagonals of $\mathbf{R}$ given by R_i [*Funning et al.*, 2005]. This value, r_i, is used to visualize the spatial interdependence of model parameters.

A comparison of our checkerboard testing and the resolution spread parameter is shown in Figure 4. We assign "good" recoverability where the original checkerboard shape can be distinguished, as opposed to locations in which the checkerboard is smeared beyond recognition. Beneath the 40 postseismic GPS sites at approximately 15–20 km spacing on the Nicoya Peninsula there is excellent recoverability over the western coast of the peninsula. Denoted by the thick purple line in Figure 4b, the maximum zone of recoverability extends to within ~30 km of the trench and matches approximately with the 25 km resolution contour. This line denotes the points at which parameters on one patch have a trade-off with parameters on patches in the surrounding 25 km. Any slip outside of this region cannot be appropriately estimated with this data set and smoothing.

3. Results and Discussion

3.1. Surface Displacements

For the period for which we have the most complete GPS coverage, 2012–2015, GPS-determined horizontal surface displacements are primarily trenchward with offsets between 7 and 26 cm. As described in *Wang et al.* [2012], we expect that afterslip will cause wholesale seaward motion, while viscoelastic relaxation should

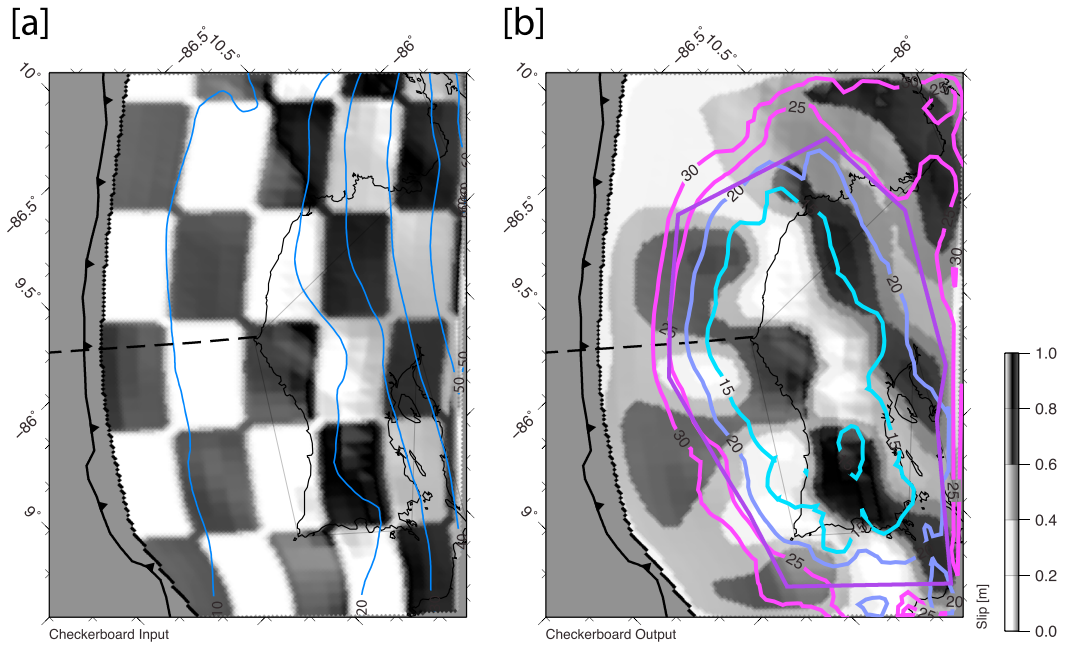

Figure 4. Results of checkerboard recoverability testing for (a) input model and (b) resultant slip using preferred smoothing value (κ = 9000). Depth contours are overlain in blue over input slip panel. Output slip panel shows annotated contours of resolvability (in km) as well as a dark purple, angular polygon surrounding area for which there is good recoverability based on checkerboard test. For more information about resolution and recoverability tests please see section 2.2. EPR-CNS suture shown as dashed line, MAT as solid line with teeth.

increasingly push coastal stations landward and inland stations seaward. Accordingly, any seaward motion of coastal sites is likely to be the result of afterslip rather than relaxation. Large seaward displacements near the coast suggest that afterslip is occurring, and at least in the shallow subduction zone, may be a dominant mechanism operating over this period.

Comparing velocities over the last year of observation (Table 2) to late interseismic velocities of 15–25 mm/yr NNE [*Feng et al.*, 2012, Table 1], we identify that a transition to preseismic convergence rates has not yet occurred. As megathrust coupling reinitiates we should again expect to observe a transition from seaward to landward surface velocities, that should eventually approximate the prior interseismic rates, with clear landward motion initiating at coastal sites and propagating inland [*Wang et al.*, 2012]. In contrast, the 2015–2016 period shows dominantly trench-parallel motion of 4–27 mm/yr NW. Convergence, though not yet returned to interseismic rates, suggests that afterslip is ceasing and that there are likely overlapping contributions from minor continued afterslip, early relocking, and viscoelastic relaxation to the observed surface deformation field.

3.2. Afterslip Inversion

We explored a range of κ values for this inversion (Figure 5), choosing the preferred κ value of 9000 near the inflection point in our models. This point is similar in both the freely sliding and fixed surface models, because deviations in model results primarily occur in the near-trench environment where our data are insensitive to model variability; differences in parameters are outside of the area of recoverability. To demonstrate the effect of oversmoothing or undersmoothing, Figure 5 includes slip results for κ of 4000 and 18,000, inset top right. While the maximum amount of slip varies only slightly between these three models, the rougher solution contains several segments of slip in small patches, while the smoother solution averages slip over large areas to produce a map with only three slipping patches. The two patches of slip on the seaward coast of the peninsula remain in all three cases and are considered robust. Only the preferred result will be discussed further. We compare our observed surface displacements with those predicted from the freely sliding trench inversion (Figure 6). Generally, the horizontal displacements are well matched while the smaller vertical vectors are more variable. Results are similar for the fixed surface model (Figure S2).

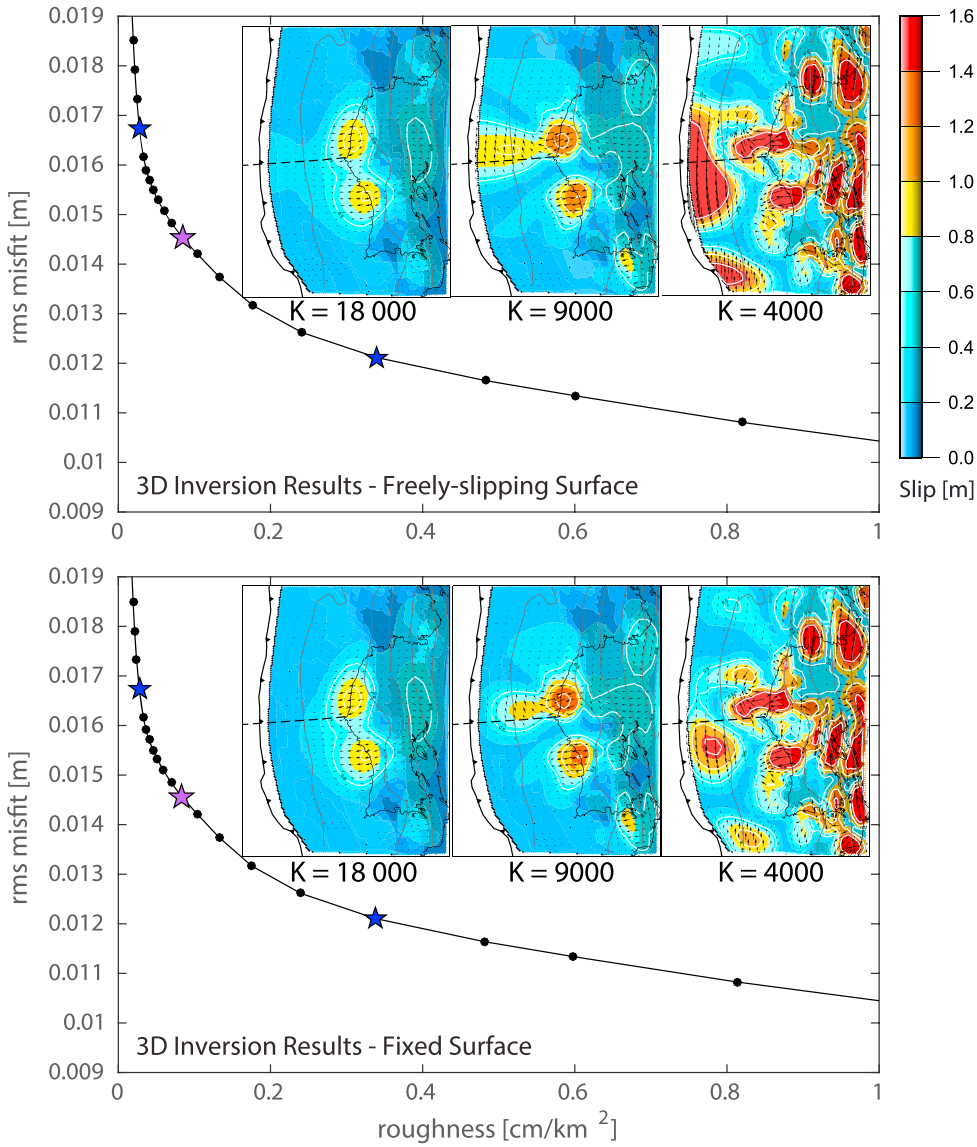

Figure 5. Roughness versus misfit for inversion of 2012–2015 GPS displacements. Preferred solution of $\kappa = 9000$ indicated by purple star. The blue stars indicate undersmoothed and oversmoothed solutions of $\kappa = 4000$ and 18,000. Resulting maps of afterslip are shown as insets. From left to right they represent oversmoothed, preferred, and undersmoothed results.

Within the zone of recoverability, slip inversion results display a maximum of 1.7 m of reverse slip. This is true of both the freely slipping and fixed trench surface cases (Figures 7 and 8, respectively). Fixed and freely slipping boundary conditions both have a cumulative postseismic slip moment (M_o) of 2.0×10^{20} Nm (M_w 7.5) inside the zone of recoverability, assuming rigidity of 30 GPa, with comparable RMS residuals (14.54 and 14.56 mm; Figure 5). The primary difference between these cases lies outside of the zone of recoverability (denoted by thick purple line in Figures 7 and 8), with more shallow slip suggested by the freely slipping trench case. While we do not have data sufficiently close to the trench to determine the existence of slip there, *Davis et al.* [2015] use pressure changes from the time of the main shock until the end of 2013 to estimate up to 0.76 m of postseismic slip at the toe. We therefore consider these two results as end-members but prefer the freely slipping (nonfixed) trench model (Figure 7).

Three patches of significant afterslip both updip and downdip of the coseismic rupture area (pink contour) are imaged in Figures 7b and 8b. The strongest slip is near the coastline in two distinct patches at roughly 15–20 km depth on either side of the EPR-CNS transition, with some slip extending seaward along the transition. Downdip there is a diffuse zone of up to 0.7 m slip, running parallel to strike between roughly 25–50 km

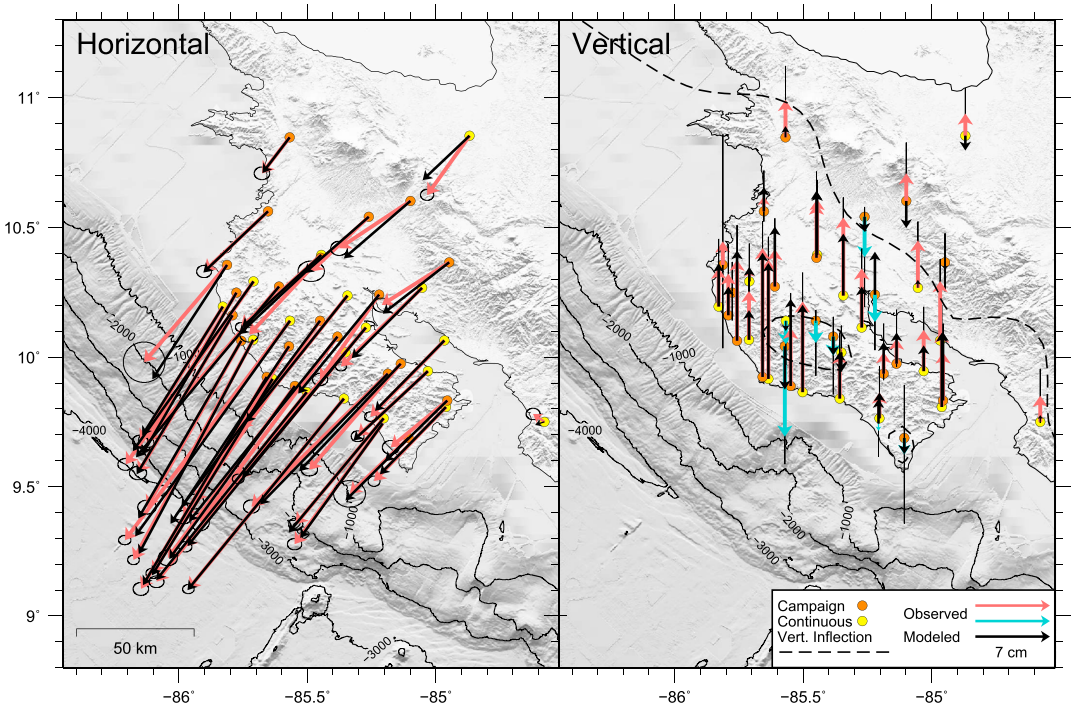

Figure 6. GPS displacements for 2012–2015 time period, shown for comparison against model predictions for preferred slip result with free surface. Observations shown by colored arrows, with predictions indicated by black arrows. (left) Horizontal displacement; (right) vertical displacement. The dashed line in Figure 6 (right) shows modeled zero vertical deformation, separating uplift from subsidence.

depth. Lastly, a region of slip is imaged in the south end of the zone of recoverability, beneath the Gulf of Nicoya, with a maximum of 0.9 m of slip at 15–40 km depth.

3.3. Comparison to Aftershocks

Afterslip is a response to unrelieved interseismic stress and any additional coseismically induced stresses that are commonly thought to at least partially drive aftershocks [e.g., *Hsu et al.*, 2006; *Chan and Stein*, 2009; *Helmstetter and Shaw*, 2009]. If coseismic slip is assumed to drive postseismic behavior, then the occurrence of either aftershocks or afterslip is likely the result of differing frictional parameters on the fault surface. Afterslip is thought to be the preferred release mechanism for velocity-strengthening materials whereas aftershocks nucleate where the surface is velocity-weakening [e.g., *Marone et al.*, 1991; *Helmstetter and Shaw*, 2009]. This hypothesis requires the observed postseismic behaviors to be spatially separated at any point in time. To explore the veracity of this idea in the current case, we compare our preferred afterslip model with the aftershock distribution of *Yao et al.* [2017]. This catalog contains 7747 events over 4 months from the 5 September main shock to the end of 2012, with local magnitudes (M_L) up to 5.7 (corresponding to the largest M_w 6.4 aftershock). To reduce noise associated with more poorly determined events, we evaluate a subset of the catalog with a minimum of 10 associated *P* and *S* wave arrivals, each, and a formal RMS error of less than the average plus one standard deviation. The resulting subset of 5381 events is plotted in Figures 7a and 8a, along with the repeating earthquakes of *Yao et al.* [2017].

Near the peninsula, the majority of aftershocks are concentrated in clusters immediately southeast of the EPR-CNS boundary near the "elbow" of the coastline and at the southern tip of the peninsula near Cabo Blanco Park. Notably, both aftershock clusters have experienced episodic tremor prior to the 2012 earthquake [*Walter et al.*, 2011]. Areas of strong updip afterslip near the coastline are bounded laterally by aftershock clusters, with little aftershock activity in the regions of greatest afterslip. A similar anticorrelation of aftershocks and afterslip was previously observed for the 2004 Parkfield and 2005 Nias earthquake [*Hsu et al.*, 2006], with the former being interpreted as the result of frictional properties that vary along strike [*Barbot et al.*, 2009]. It is likely that the same is occurring at Nicoya over depths of 15–20 km where the anticorrelation is strongest. Almost all repeating earthquakes are located in this same depth range, although they

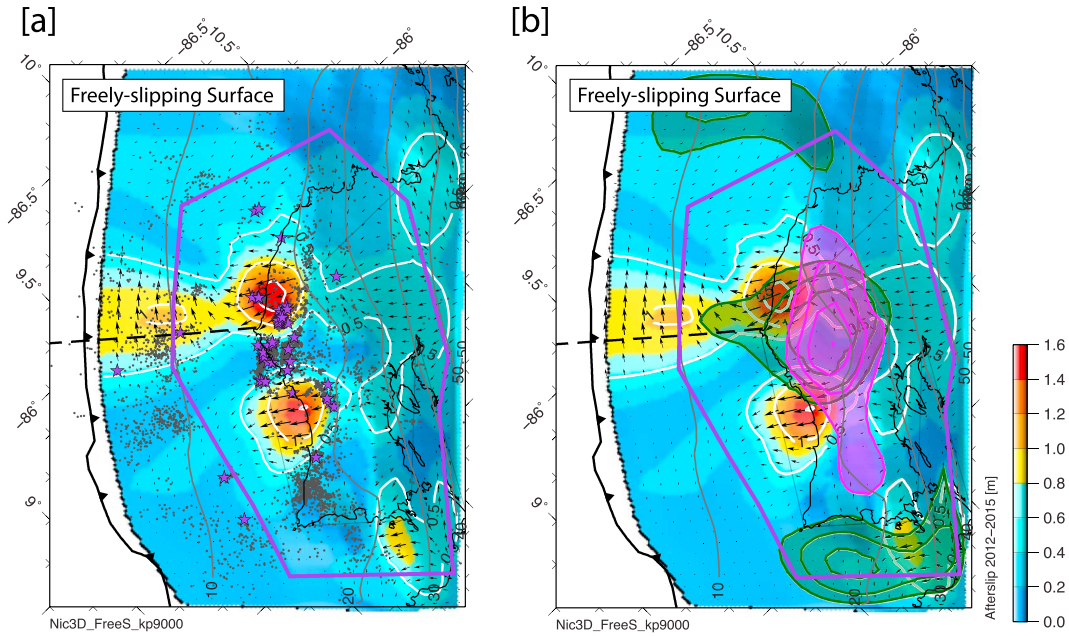

Figure 7. Both panels show result of 2012–2015 inversion where slip is allowed at the trench (nonfixed surface). Magnitude of total postseismic slip on the subduction interface is scaled by color, with arrows showing direction of hanging wall motion at each patch. The white lines show 50 cm contours of slip. The thick black line with teeth marks the Middle America Trench, while the thin grey lines show depth in 10 km intervals [*Kyriakopoulos et al.*, 2015]. The dashed line shows EPR-CNS transition [*Barckhausen et al.*, 2001]. The purple polygon denotes zone of recoverability, outside of which we are unable to resolve structures uniquely. (a) Aftershocks until end of 2012 shown as grey dots, with purple stars representing locations of repeating aftershock clusters [*Yao et al.*, 2017]. (b) The 2012 coseismic slip contours shown in pink (every 100 cm), with percentage of pre-2012 locking annotated and shown in green (20% intervals, starting at 50%) [*Kyriakopoulos and Newman*, 2016].

also appear to be anticorrelated with strong afterslip. This is an unexpected finding, given that the current literature on repeating earthquakes suggests that they are commonly the result of small patches of slip-weakening material embedded within a broader slip-strengthening region [e.g., *Nadeau and McEvilly*, 1999; *Beeler et al.*, 2001; *Chen and Lapusta*, 2009]. The notion that these repeaters are the result of surrounding aseismic slip has even been implemented by *Uchida and Matsuzawa* [2013] to use repeating aftershocks as a proxy for afterslip following the 2011 M_w 9.0 Tohoku-Oki earthquake. It appears, however, that this technique is not uniformly applicable to all small, repeating aftershocks.

Over the coseismic depth range of roughly 20–30 km we see more distributed aftershocks occurring, albeit with a lower density of events than immediately above. This is consistent with a sustained velocity-weakening behavior in the seismogenic zone over the postseismic period. The shallowest 10 km of the subduction interface also experiences diffuse but poorly located aftershocks, while in the 10–15 km and 30–50 km range there is little observed seismicity and only modest afterslip. Total moment from aftershocks is not calculated [*Yao et al.*, 2017], but their contribution to slip is included in estimates herein.

Interseismic seismicity, as recorded by the CRSEIZE experiment [*DeShon et al.*, 2006], is more dispersed along strike despite the majority of interplate events also locating between 15 and 20 km depth. This suggests that slip-strengthening behavior may be ephemeral at this depth, being initiated by the 2012 earthquake.

3.4. Comparison to Interseismic and Coseismic Slip

When examining the entire seismic cycle "slip budget" on the subduction interface, it is crucial to consider the spatial relationship of locking, coseismic slip, and afterslip. In the along-dip direction, afterslip occurs both above and below the coseismic slip region, with maximum afterslip (1.7 m) nearly one-half of the observed coseismic slip (4 m) [*Kyriakopoulos and Newman*, 2016]. Likewise, the moment released by afterslip within the region of recoverability ($M_o = 2.0 \times 10^{20}$ Nm, M_w 7.5) is about one-half of that observed coseismically ($M_o = 3.7 \times 10^{20}$ Nm, M_w 7.6) [*Kyriakopoulos and Newman*, 2016]. Following the 2012 earthquake, *Protti et al.* [2014] observed that a portion of the interseismically locked area just offshore remained unruptured during

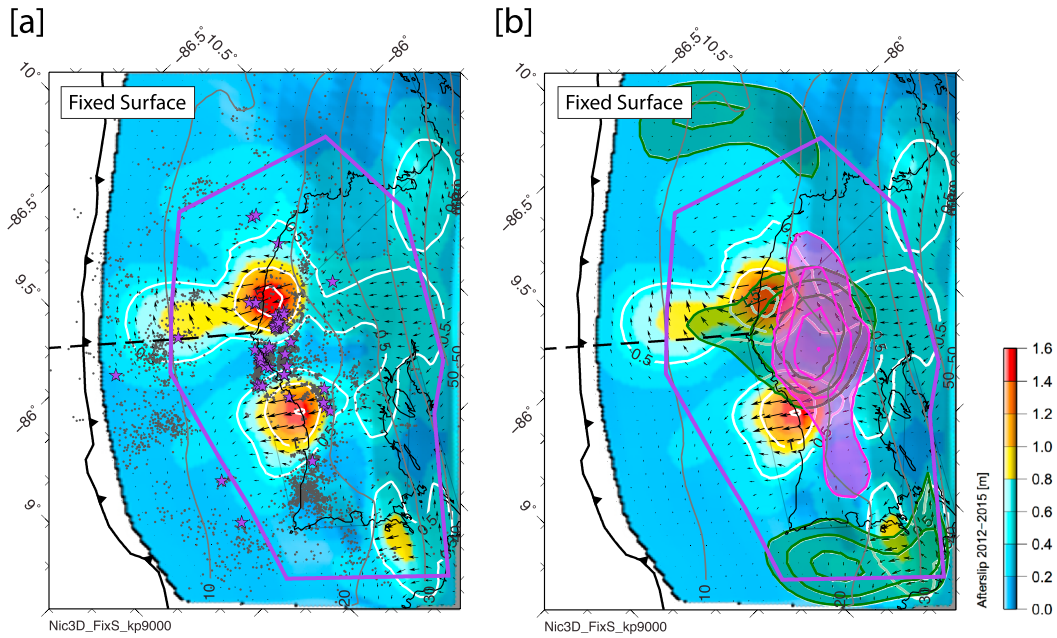

Figure 8. Same as for Figure 7 except with inversion not allowing slip to rupture the trench (fixed surface). Again, slip on the subduction interface is scaled by color, with arrows showing direction of hanging wall motion at each patch. The white lines show 50 cm contours of slip. The purple polygon denotes zone of recoverability, outside of which we are unable to resolve structures uniquely. (a) Aftershocks until end of 2012 shown as grey dots, with purple stars representing locations of repeating aftershock clusters [*Yao et al.*, 2017]. (b) The 2012 coseismic slip contours shown in pink (every 100 cm), with percentage of pre-2012 locking annotated and shown in green (20% intervals, starting at 50%) [*Kyriakopoulos and Newman*, 2016].

the main shock (Figures 7b and 8b). While we observe that a large segment has slipped during the postseismic phase, a portion appears to remain locked. To quantify this, we estimate the spatial distribution of slip deficit since the most recent prior Nicoya megathrust earthquake.

Using the interseismic locking model of *Kyriakopoulos and Newman* [2016; based on *Feng et al.*, 2012] and a constant convergence at 83 mm/yr [*DeMets et al.*, 2010], the maximum accumulated slip from 1950 to 2012 in regions of 100% coupling is estimated to be 5.15 m. From this we subtract coseismic slip [*Kyriakopoulos and Newman*, 2016; based on *Protti et al.*, 2014] and our preferred afterslip model. The total remaining moment at seismogenic depths between 10 and 30 km is $M_o = 2.0 \times 10^{20}$ Nm (M_w 7.5) and includes contributions from several patches (Figure 9). This value is likely an overestimate as it does not explicitly account for slip associated with intermediate sized earthquakes (e.g., 1978 and 1990) and assumes the late-interseismic locking as observed between about 2000 and 2010 to be constant through the interseismic period. Furthermore, SSEs, which are implicitly included if they occurred during the observed late-interseismic period, may too change over time. Beneath most of the peninsula, it appears that interseismic strain energy is largely relieved by coseismic and postseismic slip, with $<$1 m residuals. However, a large slip deficit ($>$3 m) remains within the southeastern edge of the zone of recoverability. This overlaps a region of frequent slow slip (discussed in following section) and the 1990 M_w 7.0 earthquake at the entrance to the Gulf of Nicoya [*Protti et al.*, 1995], which likely accounts for some of the deficit reported here.

Directly beneath the elbow of the peninsula (Punto Guiones), the approximate transition between EPR and CNS crust and the location of intense aftershock seismicity, we find that more than 2 m of slip deficit still remains. As an update from the *Protti et al.* [2014] result, we find the patch of unresolved slip near Punto Guiones to have 5.3×10^{19} Nm of unrecovered moment, capable of up to an M_w 7.1 earthquake (indicated by pink polygon, Figure 9). While such an event certainly has an increased tsunami potential over the prior underland rupture in 2012, we suspect that it is unlikely to extend significantly toward the trench like the destructive 1992 Nicaragua tsunami earthquake that occurred immediately northwest of the Nicoya Peninsula [e.g., *Kanamori and Kikuchi*, 1993; *Satake et al.*, 1993; *Ihmlé*, 1996]. The lack of significant seismogenic coupling in this region, supported by seafloor pressure data of *Davis et al.* [2015], suggests that slip is being relieved aseismically near the trench.

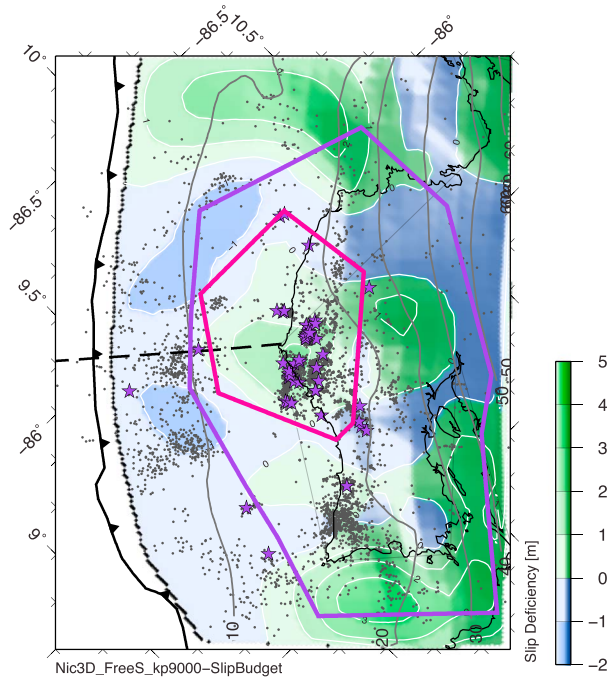

Figure 9. Slip deficit as difference between interseismic locking, coseismic slip, and afterslip. Interseismic slip accumulation is calculated as percentage of interseismic locking [*Kyriakopoulos and Newman*, 2016] multiplied by the full tectonic convergence rate over 62 years. Afterslip is from nonfixed surface model. Negative slip deficit represents slip overshoot. Overlain are aftershocks and repeating events from Figures 6a and 7a [*Yao et al.*, 2017]. The pink polygon shows the region of significant stored strain near the elbow in the coastline, as discussed in section 3.4. The purple polygon shows area of recoverability, the dashed black line is EPR-CNS transition from *Barckhausen et al.* [2001], and the thick black line with teeth marks the Middle America Trench.

3.5. Comparison to Slow Slip

The approximately 0.8 m of afterslip at the southernmost, downdip extent of the peninsula near the entrance to the Gulf of Nicoya, though possibly biased by the edge of the model, is intriguing. Nearby continuous GPS sites show a clear temporary reversal in very early 2014 and another potential event in 2015 (Figures 3 and S3)—transient southwestward displacement consistent with the direction of coseismic, postseismic, and previous SSE displacements. This location has experienced SSEs in 2007, 2009, and 2012 prior to and concurrent with the Nicoya earthquake [*Dixon et al.*, 2014]. *Voss et al.* [2017] find up to 0.14 m slip in the Gulf of Nicoya area during the 2014 SSE, accounting for only 18% of the observed afterslip in the Gulf. This suggests that afterslip and SSEs are both occurring in this region, which may be associated with a subducting seamount that nucleated the 1990 M_w 7.0 earthquake in the Gulf of Nicoya [*Husen et al.*, 2002].

Frequent aseismic slips along the Nicoya margin may help relieve stored strain energy and is likely tied to elevated fluid pressures. Extremely high V_p/V_s [*Audet and Schwartz*, 2013] and abruptly reduced seismic velocities following the 2012 main shock [*Chaves and Schwartz*, 2016] indicate fore-arc pore pressures that may approach lithostatic, effectively weakening the upper plate and allowing SSEs approximately every 1–2 years unless loaded coseismically [*Audet and Schwartz*, 2013; *Dixon et al.*, 2014].

3.6. Potential Anelastic Contributions

An elongate and diffuse region of up to 0.7 m of slip is observed near the downdip edge of the study region, with slip at depth greater than 30 km accounting for 22% of the total afterslip moment within the zone of recoverability. While our modeled slip may accurately represent elastic behavior of the subduction interface just downdip of coseismic slip, it is also likely that there is an appreciable anelastic contribution. *Malservisi et al.* [2015] found that the 2 year postseismic GPS time series across 18 continuous stations on the peninsula are well fit by combined relaxation functions with characteristic timescales of 7, 70, and greater than 400 days, suggesting contributions from poroelastic deformation, afterslip, and downdip viscoelastic relaxation, respectively. We identify that this idea is supported by the paucity of aftershock activity below ~30 km depth (Figures 7b and 8b), although the CRSEIZE experiment recorded seismicity at these depths during the interseismic period [*DeShon et al.*, 2006]. A detailed tomographic model, developed by *DeShon et al.* [2006], estimated that the Mohorovičić discontinuity intersects the slab at 30–40 km beneath Nicoya, updip of our observed deep afterslip.

Postseismic viscoelastic relaxation is expected following large megathrust events, though the relative proportions of relaxation and afterslip are difficult to determine due to their shared seaward motion of the upper plate [*Wang et al.*, 2012]. Because the current model assumes that all deformation is on-fault and elastic,

we are similarly unable to resolve between deep fault slip and distributed relaxation of the upper mantle. Estimates herein of deep afterslip should therefore be taken as an end-member behavior. Evaluating the anelastic component of postseismic deformation will become increasingly important when considering longer time periods leading toward relocking of the megathrust.

Similarly, this model also makes no attempt to model poroelastic relaxation. While *Malservisi et al.* [2015] posit a short-period relaxation signal consistent with poroelastic effects, modeled displacements from poroelastic rebound were found to be significantly smaller than the displacements associated with that 7 day relaxation and directionally inconsistent with poroelastic stressing. We suspect that the poroelastic effect is likely to be only a modest contribution as compared to the dominant afterslip signal observed over the 2.5-year period.

3.7. Spatially Variable Fault Behavior on the Nicoya Megathrust

Synthesizing all of our observations about slip, there are substantial differences in afterslip along strike and dip. At the 15–20 km depth range along the entire Nicoya Peninsula, postseismic activity appears as either afterslip with little seismicity or as aftershock clusters with little observed cumulative slip. Given that this band experiences spatially similar loading by stress heterogeneities at the edge of the coseismic rupture area, such variable slip behavior along strike must be the result of changes in thermal, geological, frictional, and/or structural regime.

The thermal state of the Nicoya Peninsula is dominantly controlled by the change in provenance of the oceanic crust between relatively warm CNS and abnormally cold EPR material [*Harris and Wang*, 2002; *Hutnak et al.*, 2007]. Afterslip and aftershocks nucleating at the same depth along the southern CNS crust, where temperatures should be fairly constant, suggest that the spatial separation of afterslip and aftershocks at the same depth is not significantly thermally controlled. Similarly, hanging wall lithology is consistent in the along-strike direction across the Nicoya Peninsula [*Bourgois et al.*, 1984] and subducting crusts are similar ages even across the EPR-CNS suture [*Barckhausen et al.*, 2001]. This suggests no substantial age-related or lithologic control.

Rate-and-state friction dictates that when a sufficient stress is applied to a fault it will fail seismically or aseismically depending on whether the interface material is velocity-weakening or velocity-strengthening, respectively [e.g., *Dieterich*, 1972; *Ruina*, 1983; *Scholz*, 1998]. If the subduction interface is velocity-weakening near Punto Guiones (elbow in coastline), it would resist slipping aseismically and instead nucleate aftershocks in a region surrounded by stress heterogeneities in the downdip and lateral directions. A similar contrast in frictional parameters in the along strike direction was previously observed by *Barbot et al.* [2009] for the 2004 Parkfield earthquake, where afterslip was anticorrelated with aftershocks, and explains the disconnected nature of afterslip patches near the coast.

Other than the clear transition in material origin and thermal state across the downgoing plate, the only other notable difference is the existence of "subducted topography" along the interface associated with the CNS crust [*Kyriakopoulos et al.*, 2015]. As discussed in *Yao et al.* [2017], aftershock clusters occur along and possibly within the microseismically defined indenters immediately south of the elbow in the coast (the focus of most coseismic rupture in 2012), as well as near the continuation of the Fisher Seamount chain subducting at the southernmost tip of the peninsula near Cabo Blanco (just north of the 1990 earthquake, indicated in Figure 1) [*Kyriakopoulos et al.*, 2015]. Subducted seamounts, the most commonly discussed indenter, are often associated with abundant microseismicity and occasionally larger earthquakes with complex rupture patterns [*Wang and Bilek*, 2011]. In the current study, we note that coseismic slip and aftershock activity appear to terminate above approximately 20 km depth, except in zones of significant slab topography, suggesting that topography primarily affects the updip extent of aftershock behavior.

3.8. Continuing Postseismic Deformation

Visual inspection of continuous GPS time series shows that the postseismic response curve has flattened for many sites (Figure 3), suggesting that afterslip and postseismic relaxation may be approaching completion by 2015 [e.g., *Wang et al.*, 2012]. Continued observations are critical as the landward velocities increase toward interseismic values. This process may begin at the toe of the subduction zone and propagate inland, as is now observed in Chile following the 1960 M_w 9.5 Valdivia earthquake [*Wang et al.*, 2007], rendering coastal observations particularly crucial for understanding the exact timing of relocking. This coastal initiation of landward motion is thought to be from superposition of both interseismic plate convergence and

postseismic viscoelastic relaxation, which is expected to be landward at coastal stations and seaward at inland stations due to the opposing directions of relaxation between the oceanic mantle and mantle wedge [*Wang et al.*, 2012]. Because stress-related postseismic processes largely overlap both temporally and spatially, including afterslip, aftershocks, poroelastic, and viscoelastic relaxation, it is difficult to uniquely isolate their individual contributions, particularly when the timescales of some behaviors may be stress-dependent [e.g., *Bürgmann and Dresen*, 2008]. This can become further complicated later in the postseismic cycle as portions of the interface begin to relock, while others still slip, and postseismic relaxation processes are ongoing —this is where we find Nicoya in 2015.

Keeping an updated budget of potential slip during the next megathrust event will improve seismic hazard assessments. Current GPS monument configuration may also prove useful for determining the spatiotemporal evolution of the early interseismic period, wherein the width of the locked seismogenic zone is expected to narrow as downdip frictional locking decreases [*Wang and Tréhu*, 2016]. Evaluating more complex models (e.g., viscoelastic and pore pressure response and rate-and-state friction law) has improved our understanding of the crustal and mantle response to rapid coseismic loading [e.g., *Jónsson et al.*, 2003; *Barbot et al.*, 2009; *Johnson et al.*, 2009; *Hu et al.*, 2016]. Given the ideal geometry and rich data across the Nicoya Peninsula, application of such models to this data set should provide quantitative estimates of the mantle rheology and characteristic timescale of recovery for Nicoya, ideal for comparison with measurements of megathrusts worldwide.

4. Conclusions

Using three and a half years of dense GPS measurements following the 5 September 2012 M_w 7.6 Nicoya Peninsula, Costa Rica, earthquake, we identify distinct pattern spatial and temporal evolution of postseismic deformation. Strong seaward displacements occur over the first 2.5 year period and diminish to almost zero trench-normal velocities by mid-2016. This indicates that relocking has initiated, but GPS velocities have yet to return to interseismic rates observed in the decade prior to the main shock.

Modeled afterslip, using the 3-D subduction interface model of *Kyriakopoulos et al.* [2015], found up to 1.7 m of motion in two slip patches immediately updip of coseismic rupture, below the western coast of the peninsula. Comparison with afterslip results from a model using the 2-D geometry (Figure S1 and accompanying text) are similar with the 3-D results presented herein, suggesting that the observed slip distribution is not an artifact of complex model geometry. Aftershock seismicity occurs in two clusters: between these coastal afterslip patches and directly southeast of the southern patch, forming a 15–20 km deep band of strong postseismic activity running the entire length of the peninsula. Differences in behavior along this band may be tied to varying frictional properties and/or the distribution of subducted topography. A region of deeper slip imaged at the downdip edge of coseismic rupture may be real or could be the result of unmodeled viscoelastic relaxation. At the southeast edge of the study area, near the Gulf of Nicoya, another patch of significant afterslip exists near the locus of several slow-slip events. One such event in 2014 is thought to account for less than 20% of the cumulative slip in this region; thus, significant afterslip is still required to explain most deformation.

Ultimately, afterslip and aftershocks are spatially distinct, and primarily outline the updip edge of the 2012 coseismic rupture. While some aftershocks are seen to be repeating [*Yao et al.*, 2017], the spatial distribution of aftershock behavior is insufficient to describe the afterslip signal.

Future measurements with this network will provide insights about the relocking and early interseismic behavior along this megathrust. Such details are useful for comparison with other subduction zones without such favorable land geometry, as well as for estimation of seismic and tsunami hazard in Costa Rica as the Nicoya megathrust enters another seismic cycle.

Acknowledgments
NSF funding to A.V.N. through 1447104 and 1262267. NSERC funding to T.E.H. through PGSD2-488063-2016. Raw continuous and campaign GPS are available at UNAVCO.org. Model outputs are available at http://nicoya.eas.gatech.edu. Fieldwork would not have been possible without the help of B. Burgoa, K. Gardner, M. Kemmerlin, A. Williamson, and J. McAdams. We thank T. Dixon for valuable input in shaping this manuscript, as well as thorough reviews from J. Hsu and three anonymous reviewers.

References

Altamimi, Z., X. Collilieux, and L. Métivier (2011), ITRF2008: An improved solution of the international terrestrial reference frame, *J. Geod.*, *85*(8), 457–473.

Audet, P., and S. Y. Schwartz (2013), Hydrologic control of forearc strength and seismicity in the Costa Rican subduction zone, *Nat. Geosci.*, *6*(10), 852–855.

Barbot, S., Y. Fialko, and Y. Bock (2009), Postseismic deformation due to the M_w 6.0 2004 Parkfield earthquake: Stress-driven creep on a fault with spatially variable rate-and-state friction parameters, *J. Geophys. Res.*, *114*, B07405, doi:10.1029/2008JB005748.

Barckhausen, U., C. R. Ranero, R. V. Huene, S. C. Cande, and H. A. Roeser (2001), Revised tectonic boundaries in the Cocos Plate off Costa Rica: Implications for the segmentation of the convergent margin and for plate tectonic models, *J. Geophys. Res.*, *106*(B9), 19,207–19,220, doi:10.1029/2001JB000238.

Beeler, N. M., D. L. Lockner, and S. H. Hickman (2001), A simple stick-slip and creep-slip model for repeating earthquakes and its implication for microearthquakes at Parkfield, *Bull. Seismol. Soc. Am.*, *91*(6), 1797–1804.

Blewitt, G. (2008), Fixed point theorems of GPS carrier phase ambiguity resolution and their application to massive network processing: Ambizap, *J. Geophys. Res.*, *113*, B12410, doi:10.1029/2008JB005736.

Bourgois, J., J. Azema, P. O. Baumgartner, J. Tournon, A. Desmet, and J. Aubouin (1984), The geologic history of the Caribbean-Cocos Plate boundary with special reference to the Nicoya ophiolite complex (Costa Rica) and DSDP results (Legs 67 and 84 off Guatemala): A synthesis, *Tectonophysics*, *108*(1–2), 1–32.

Bürgmann, R., and G. Dresen (2008), Rheology of the lower crust and upper mantle: Evidence from rock mechanics, geodesy, and field observations, *Annu. Rev. Earth Planet. Sci.*, *36*, 531–567, doi:10.1146/annurev.earth.36.031207.124326.

Chan, C. H., and R. S. Stein (2009), Stress evolution following the 1999 Chi-Chi, Taiwan, earthquake: Consequences for afterslip, relaxation, aftershocks and departures from Omori decay, *Geophys. J. Int.*, *177*(1), 179–192.

Chaves, E. J., and S. Y. Schwartz (2016), Monitoring transient changes within overpressured regions of subduction zones using ambient seismic noise, *Sci. Adv.*, *2*(1), e1501289.

Chen, T., and N. Lapusta (2009), Scaling of small repeating earthquakes explained by interaction of seismic and aseismic slip in a rate and state fault model, *J. Geophys. Res.*, *114*, B01311, doi:10.1029/2008JB005749.

Chen, T., A. V. Newman, L. Feng, and H. M. Fritz (2009), Slip distribution from the 1 April 2007 Solomon Islands earthquake: A unique image of near-trench rupture, *Geophys. Res. Lett.*, *36*, L16307, doi:10.1029/2009GL039496.

Davis, E. E., H. Villinger, and T. Sun (2015), Slow and delayed deformation and uplift of the outermost subduction prism following ETS and seismogenic slip events beneath Nicoya Peninsula, Costa Rica, *Earth Planet. Sci. Lett.*, *410*, 117–127.

DeMets, C., R. G. Gordon, and D. F. Argus (2010), Geologically current plate motions, *Geophys. J. Int.*, *181*(1), 1–80.

DeShon, H. R., S. Y. Schwartz, A. V. Newman, V. González, M. Protti, L. M. Dorman, T. Dixon, D. E. Sampson, and E. R. Flueh (2006), Seismogenic zone structure beneath the Nicoya Peninsula, Costa Rica, from three-dimensional local earthquake P-and S-wave tomography, *Geophys. J. Int.*, *164*(1), 109–124.

Dieterich, J. H. (1972), Time-dependent friction in rocks, *J. Geophys. Res.*, *77*(20), 3690–3697, doi:10.1029/JB077i020p03690.

Dinc, A. N., I. Koulakov, M. Thorwart, W. Rabbel, E. R. Flueh, I. Arroyo, W. Taylor, and G. Alvarado (2010), Local earthquake tomography of central Costa Rica: Transition from seamount to ridge subduction, *Geophys. J. Int.*, *183(1)*, 286–302.

Dixon, T. H., Y. Jiang, R. Malservisi, R. McCaffrey, N. Voss, M. Protti, and V. Gonzalez (2014), Earthquake and tsunami forecasts: Relation of slow slip events to subsequent earthquake rupture, *Proc. Natl. Acad. Sci.*, *111*(48), 17,039–17,044.

Ekström, G., M. Nettles, and A. M. Dziewoński (2012), The global CMT project 2004–2010: Centroid-moment tensors for 13,017 earthquakes, *Phys. Earth Planet. Inter.*, *200*, 1–9.

Feng, L., A. V. Newman, M. Protti, V. Gonzalez, Y. Jiang, and T. H. Dixon (2012), Active deformation near the Nicoya Peninsula, northwestern Costa Rica, between 1996 and 2010: Interseismic megathrust coupling, *J. Geophys. Res.*, *117*, B06407, doi:10.1029/2012JB009230.

Funning, G. J., B. Parsons, T. J. Wright, J. A. Jackson, and E. J. Fielding (2005), Surface displacements and source parameters of the 2003 Bam (Iran) earthquake from Envisat advanced synthetic aperture radar imagery, *J. Geophys. Res.*, *110*, B09406, doi:10.1029/2004JB003338.

Gubbins, D. (2004), The under-determined problem, in *Time Series Analysis and Inverse Theory for Geophysicists*, pp. 110–124, Cambridge Univ. Press, Cambridge, U. K.

Harris, R. N., and K. Wang (2002), Thermal models of the middle America trench at the Nicoya Peninsula, Costa Rica, *Geophys. Res. Lett.*, *29*(21), 2010, doi:10.1029/2002GL015406.

Harris, R. N., G. Spinelli, C. R. Ranero, I. Grevemeyer, H. Villinger, and U. Barckhausen (2010), Thermal regime of the Costa Rican convergent margin: 2. Thermal models of the shallow middle America subduction zone offshore Costa Rica, *Geochem. Geophys. Geosyst.*, *11*, Q12S29, doi:10.1029/2010GC003273.

Helmstetter, A., and B. E. Shaw (2009), Afterslip and aftershocks in the rate-and-state friction law, *J. Geophys. Res.*, *114*, B01308, doi:10.1029/2007JB005077.

Hsu, Y. J., M. Simons, J. P. Avouac, J. Galetzka, K. Sieh, M. Chlieh, D. Natawidjaja, L. Prawirodirdjo, and Y. Bock (2006), Frictional afterslip following the 2005 Nias-Simeulue earthquake, Sumatra, *Science*, *312*(5782), 1921–1926.

Hu, Y., K. Wang, J. He, J. Klotz, and G. Khazaradze (2004), Three-dimensional viscoelastic finite element model for postseismic deformation of the great 1960 Chile earthquake, *J. Geophys. Res.*, *109*, B12403, doi:10.1029/2004JB003163.

Hu, Y., R. Bürgmann, N. Uchida, P. Banerjee, and J. T. Freymueller (2016), Stress-driven relaxation of heterogeneous upper mantle and time-dependent afterslip following the 2011 Tohoku earthquake, *J. Geophys. Res. Solid Earth*, *121*, 385–411, doi:10.1002/2015JB012508.

Husen, S., E. Kissling, and R. Quintero (2002), Tomographic evidence for a subducted seamount beneath the Gulf of Nicoya, Costa Rica: The cause of the 1990 M_w = 7.0 Gulf of Nicoya earthquake, *Geophys. Res. Lett.*, *29*(8), 1238, doi:10.1029/2001GL014045.

Hutnak, M., et al. (2007), The thermal state of 18–24 Ma upper lithosphere subducting below the Nicoya Peninsula, northern Costa Rica margin, in *The Seismogenic Zone of Subduction Thrust Faults*, edited by T. H. Dixon and J. C. Moore, pp. 86–122, Columbia Univ. Press, New York.

Ihmlé, P. F. (1996), Monte Carlo slip inversion in the frequency domain: Application to the 1992 Nicaragua slow earthquake, *Geophys. Res. Lett.*, *23*(9), 913–916, doi:10.1029/96GL00872.

International Seismological Centre (2014), *On-line Bulletin*, Internatl. Seismol. Cent., Thatcham, U. K. [Available at http://www.isc.ac.uk.]

Jiang, Y., S. Wdowinski, T. H. Dixon, M. Hackl, M. Protti, and V. Gonzalez (2012), Slow slip events in Costa Rica detected by continuous GPS observations, 2002–2011, *Geochem. Geophys. Geosyst.*, *13*, Q04006, doi:10.1029/2012GC004058.

Johnson, K. M., R. Bürgmann, and J. T. Freymueller (2009), Coupled afterslip and viscoelastic flow following the 2002 Denali Fault, Alaska earthquake, *Geophys. J. Int.*, *176*(3), 670–682.

Jónsson, S., P. Segall, R. Pedersen, and G. Björnsson (2003), Post-earthquake ground movements correlated to pore-pressure transients, *Nature*, *424*(6945), 179–183.

Jónsson, S., H. Zebker, P. Segall, and F. Amelung (2002), Fault slip distribution of the 1999 M_w 7.1 Hector Mine, California, earthquake, estimated from satellite radar and GPS measurements, *Bull. Seismol. Soc. Am.*, *92*(4), 1377–1389.

Kanamori, H., and M. Kikuchi (1993), The 1992 Nicaragua earthquake: A slow tsunami earthquake, *Nature*, *361*, 25.

Khazaradze, G., K. Wang, J. Klotz, Y. Hu, and J. He (2002), Prolonged post-seismic deformation of the 1960 great Chile earthquake and implications for mantle rheology, *Geophys. Res. Lett.*, *29*(22), 2050, doi:10.1029/2002GL015986.

Kyriakopoulos, C., A. V. Newman, A. M. Thomas, M. Moore-Driskell, and G. T. Farmer (2015), A new seismically constrained subduction interface model for Central America, *J. Geophys. Res. Solid Earth*, *120*, 5535–5548, doi:10.1002/2014JB011859.

Kyriakopoulos, C., and A. V. Newman (2016), Structural asperity focusing locking and earthquake slip along the Nicoya megathrust, Costa Rica, *J. Geophys. Res. Solid Earth*, *121*, 5461–5476, doi:10.1002/2016JB012886.

LaFemina, P., T. H. Dixon, R. Govers, E. Norabuena, H. Turner, A. Saballos, G. Mattioli, M. Protti, and W. Strauch (2009), Fore-arc motion and Cocos Ridge collision in Central America, *Geochem. Geophys. Geosyst.*, *10*, Q05S14, doi:10.1029/2008GC002181.

Letellier, T. (2005), Etude des ondes de marée sur les plateaux continentaux, doctoral dissertation, Toulouse 3.

Liu, C., Y. Zheng, X. Xiong, R. Wang, A. López, and J. Li (2015), Rupture processes of the 2012 September 5 M_w 7.6 Nicoya, Costa Rica earthquake constrained by improved geodetic and seismological observations, *Geophys. J. Int.*, *203*(1), 175–183.

Malservisi, R., et al. (2015), Multiscale postseismic behavior on a megathrust: The 2012 Nicoya earthquake, Costa Rica, *Geochem. Geophys. Geosyst.*, *16*, 1848–1864, doi:10.1002/2015GC005794.

Marone, C. J., C. H. Scholtz, and R. Bilham (1991), On the mechanics of earthquake afterslip, *J. Geophys. Res.*, *96*(B5), 8441–8452, doi:10.1029/91JB00275.

Marshall, J. S., and R. S. Anderson (1995), Quaternary uplift and seismic cycle deformation, Peninsula de Nicoya, Costa Rica, *Geol. Soc. Am. Bull.*, *107*(4), 463–473.

Menke, W. (1989), Solution of the linear, Gaussian inverse problem, viewpoint 2: generalized inverses, in *Geophysical Data Analysis: Discrete Inverse Theory*, revised ed., pp. 61–78, Academic Press, San Diego, Calif.

Nadeau, R. M., and T. V. McEvilly (1999), Fault slip rates at depth from recurrence intervals of repeating microearthquakes, *Science*, *285*(5428), 718–721.

Newman, A. V., S. Y. Schwartz, V. Gonzalez, H. R. DeShon, J. M. Protti, and L. M. Dorman (2002), Along-strike variability in the seismogenic zone below Nicoya Peninsula, Costa Rica, *Geophys. Res. Lett.*, *29*(20), 1977, doi:10.1029/2002GL015409.

Outerbridge, K. C., T. H. Dixon, S. Y. Schwartz, J. I. Walter, M. Protti, V. Gonzalez, J. Biggs, M. Thorwart, and W. Rabbel (2010), A tremor and slip event on the Cocos-Caribbean subduction zone as measured by a global positioning system (GPS) and seismic network on the Nicoya Peninsula, Costa Rica, *J. Geophys. Res.*, *115*, B10408, doi:10.1029/2009JB006845.

Protti, M., et al. (1995), The March 25, 1990 (M_w = 7.0, M_L = 6.8), earthquake at the entrance of the Nicoya Gulf, Costa Rica: Its prior activity, foreshocks, aftershocks, and triggered seismicity, *J. Geophys. Res.*, *100*(B10), 20,345–20,358, doi:10.1029/94JB03099.

Protti, M., V. González, A. V. Newman, T. H. Dixon, S. Y. Schwartz, J. S. Marshall, L. Feng, J. I. Walter, R. Malservisi, and S. E. Owen (2014), Nicoya earthquake rupture anticipated by geodetic measurement of the locked plate interface, *Nat. Geosci.*, *7*(2), 117–121.

Ruina, A. (1983), Slip instability and state variable friction laws, *J. Geophys. Res.*, *88*(B12), 10,359–10,370, doi:10.1029/JB088iB12p10359.

Sak, P. B., D. M. Fisher, T. W. Gardner, J. S. Marshall, and P. C. LaFemina (2009), Rough crust subduction, forearc kinematics, and Quaternary uplift rates, Costa Rican segment of the Middle American Trench, *Geol. Soc. Am. Bull.*, *121*(7/8), 992–1012.

Satake, K., J. Bourgeois, K. Abe, K. Abe, Y. Tsuji, F. Imamura, Y. Lio, H. Katao, E. Noguera, and F. Estrada (1993), Tsunami field survey of the 1992 Nicaragua earthquake, *Eos. Trans. AGU*, *74*(13), 145–157.

Scholz, C. H. (1998), Earthquakes and friction laws, *Nature*, *391*(6662), 37–42.

Uchida, N., and T. Matsuzawa (2013), Pre-and postseismic slow slip surrounding the 2011 Tohoku-oki earthquake rupture, *Earth Planet. Sci. Lett.*, *374*, 81–91.

Vannucchi, P., D. W. Scholl, M. Meschede, and K. McDougall-Reid (2001), Tectonic erosion and consequent collapse of the Pacific margin of Costa Rica: Combined implications from ODP Leg 170, seismic offshore data, and regional geology of the Nicoya Peninsula, *Tectonics*, *20*(5), 649–668.

Voss, N. K., R. Malservisi, T. H. Dixon, and M. Protti (2017), Slow slip events in the early part of the earthquake cycle, *J. Geophys. Res. Solid Earth*, *122*, doi:10.1002/2016JB013741.

Walter, J. I., S. Y. Schwartz, J. M. Protti, and V. Gonzalez (2011), Persistent tremor within the northern Costa Rica seismogenic zone, *Geophys. Res. Lett.*, *38*, L01307, doi:10.1029/2010GL045586.

Walter, J. I., S. Y. Schwartz, M. Protti, and V. Gonzalez (2013), The synchronous occurrence of shallow tremor and very low frequency earthquakes offshore of the Nicoya Peninsula, Costa Rica, *Geophys. Res. Lett.*, *40*, 1517–1522, doi:10.1002/grl.50213.

Walter, J. I., X. Meng, Z. Peng, S. Y. Schwartz, A. V. Newman, and M. Protti (2015), Far-field triggering of foreshocks near the nucleation zone of the 5 September 2012 (M W 7.6) Nicoya Peninsula, Costa Rica earthquake, *Earth Planet. Sci. Lett.*, *431*, 75–86.

Wang, K., Y. Hu, M. Bevis, E. Kendrick, R. Smalley, R. B. Vargas, and E. Lauría (2007), Crustal motion in the zone of the 1960 Chile earthquake: Detangling earthquake-cycle deformation and forearc-sliver translation, *Geochem. Geophys. Geosyst.*, *8*, Q10010, doi:10.1029/2007GC001721.

Wang, K., and S. L. Bilek (2011), Do subducting seamounts generate or stop large earthquakes?, *Geology*, *39*(9), 819–822.

Wang, K., Y. Hu, and J. He (2012), Deformation cycles of subduction earthquakes in a viscoelastic Earth, *Nature*, *484*(7394), 327–332.

Wang, K., and A. M. Tréhu (2016), Invited review paper: Some outstanding issues in the study of great megathrust earthquakes—The Cascadia example, *J. Geodyn.*, *98*, 1–18.

Yao, D., J. I. Walter, X. Meng, T. E. Hobbs, Z. Peng, A. V. Newman, S. Y. Schwartz, and M. Protti (2017), Detailed spatio-temporal evolution of microseismicity and repeating earthquakes following the 2012 M_w7.6 Nicoya earthquake, *J. Geophys. Res. Solid Earth*, *121*, doi:10.1002/2016JB013632.

Yue, H., T. Lay, S. Y. Schwartz, L. Rivera, M. Protti, T. H. Dixon, S. Owen, and A. V. Newman (2013), The 5 September 2012 Nicoya, Costa Rica M_w 7.6 earthquake rupture process from joint inversion of high-rate GPS, strong-motion, and teleseismic P wave data and its relationship to adjacent plate boundary interface properties, *J. Geophys. Res. Solid Earth*, *118*, 5453–5466, doi:10.1002/jgrb.50379.